

Performance of Cluster Expansions of Coverage-Dependent Adsorption of Atomic Oxygen on Pt(111)

David J. Schmidt,[†] Wei Chen,[‡] C. Wolverton,[‡] and William F. Schneider^{*,†,§}

[†]Chemical and Biomolecular Engineering, University of Notre Dame, Notre Dame, Indiana 46556, United States

[‡]Material Science and Engineering, Northwestern University, Evanston, Illinois 60208, United States

[§]Chemistry and Biochemistry, University of Notre Dame, Notre Dame, Indiana 46556, United States

 Supporting Information

ABSTRACT: A density functional theory (DFT) database of 66 Pt(111)/O formation energies is presented. We fit this database of formation energies to a range of cluster expansions (CEs) of systematically increasing size and flexibility. We find that the performance of the CE depends upon the property or properties of interest. Pair-wise CEs with up to third nearest neighbor interactions poorly predict all metrics. CEs with five to eight pairwise interactions and one to two triplet interactions predicted formation energies and most ground states accurately but predicted average and differential adsorption energies with modest errors. A larger CE captures average and differential adsorption energies as well as formation energies and ground states. The choice of figures in the CEs is also examined. Pair-wise figures and the linear, 1–1–3, triplet are necessary to obtain CEs that qualitatively reproduce the examined properties; however, other figures are more interchangeable. The electronic and strain components of the adsorbate–adsorbate interactions is studied by comparing a CE of DFT formation energies in which atoms were not allowed to relax to the CEs of the relaxed surface. On an unrelaxed Pt surface, interactions are shorter-ranged interactions and more repulsive at first nearest neighbor separation.

1. INTRODUCTION

Surface adsorption is fundamental to corrosion, gas separations, chromatography, and heterogeneous catalysis. The familiar Langmuir model describes adsorption as binding of adsorbates to chemically unsaturated surface sites, and the Langmuir isotherm describes the limit that these sites are equivalent and independent. For dissociative adsorption of a diatomic adsorbate, the isotherm is given by^{1,2}

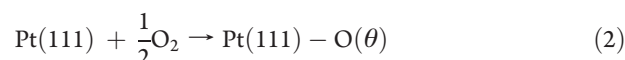


$$K(T) = \frac{\theta_{A*}^2}{P_{A_2} \theta_*^2} \quad (1b)$$

Here, each adsorbate, A, binds with the same adsorption energy at a single surface site of type, *. At equilibrium, the distribution of adsorbates among surface sites is entirely random, to maximize configurational entropy, and the equilibrium constant is written in terms of the adsorbate coverage, θ_{A*} , the vacant site coverage, θ_* , and the pressure of the diatomic adsorbate, P_{A_2} , impinging on the surface. This idealized Langmuir isotherm breaks down when adsorbate–adsorbate interactions become non-negligible.^{2–7} When adsorbate–adsorbate interactions become non-negligible, the adsorption energy of each adsorbate is influenced by its interactions with other adsorbates, and the equilibrium spatial distribution of adsorbates becomes a balance between minimizing these interaction energies and maximizing configurational entropy.

Strong adsorbate–adsorbate interactions are evident in many systems of practical interest. One that we have been particularly interested in due to its relevance to catalytic oxidations,^{8–12} as

well as the oxygen reduction reaction (ORR),¹³ is dissociative O₂ adsorption on the close-packed, hexagonal Pt(111) surface:



The (111) surface exposes face-centered-cubic (fcc) and hexagonal-close-packed (hcp) 3-fold sites, distinguished by the absence or presence of an underlying metal atom (Figure 1). Low energy electron diffraction (LEED), electron energy loss spectroscopy (EELS),¹⁴ nuclear reaction analysis (NRA), and transmission channeling (TC) experiments¹⁵ and supercell density functional theory (DFT) calculations^{11,12,16} agree that at low to moderate coverage O adsorbs preferentially in the fcc hollow sites. Temperature programmed desorption (TPD) and calorimetric experiments,^{17–19} as well as DFT calculations,^{11,12,16,20–22} agree that the interactions between these are primarily repulsive, so that adsorption energies are decreasingly exothermic with increasing coverage. Above approximately $\theta_O = 0.5$ monolayer (ML), adsorbed O begins to populate hcp sites and cause surface reconstructions that further modify adsorption energies.^{16,23}

Lateral interactions between adsorbates can also be manifested in adsorbate orderings. LEED experiments on Pt(111) crystals dosed with oxygen show p(2 × 2)-type ordering at 1/4 and 1/2 ML.^{14,17,18,24} These patterns have been ascribed to a p(2 × 2)-O ordering at 1/4 ML and the three orientations of the p(2 × 1)-O configuration at 1/2 ML.^{18,24} Similar orderings have been observed in scanning tunneling microscopy (STM)

Received: September 19, 2011

Published: December 09, 2011

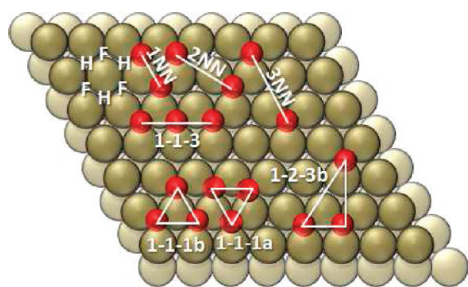


Figure 1. Schematic view of Pt(111) close-packed plane, distinguishing fcc (F) and hcp (H) sites, and illustrating representative cluster interactions.

experiments at 450 K for the $p(2 \times 2)$ -O configuration and 573 K for the $p(2 \times 1)$ -O configuration.²³

DFT calculations can be used to search for the ground states and to model coverage-dependent adsorption at metal surfaces. The Pt(111)–O system has been the subject of a number of such studies,^{11,42,16,20–22,25} recovering the coverage-dependent adsorption, predicting both the $p(2 \times 2)$ -O and $p(2 \times 1)$ -O orderings to be equilibrium ground states.^{12,16,20–22} Due to their computational cost, periodic DFT methods are limited in the sizes of supercells and thus in the range of adsorbate configurations, coverages, and adsorption energies that can be probed. An alternative to direct calculation is to develop a model energy Hamiltonian. In the first-principles cluster expansion (CE) approach,^{26–29} an Ising-type model is fit to the energies of a DFT database of adsorbate configurations. In the CE approach, the energy, E_{CE} , of an adsorbate configuration σ is expanded in polynomial “clusters” or “figures” of the spin variables σ_i .^{21,22,29–34}

$$E_{\text{CE}}(\sigma) = N_{\text{sites}}J_e + J_p \sum_i \sigma_i + \sum_{ij} J_{ij}\sigma_i\sigma_j + \sum_{ijk} J_{ijk}\sigma_i\sigma_j\sigma_k + \dots \quad (3)$$

Following the Ising convention, $\sigma_i = +1$ represents the presence and -1 the absence of an adsorbate at site i . A cluster expansion including only the empty, J_e , and point, J_p , effective cluster interactions (ECIs) corresponds to a noninteracting Langmuir model. Interactions between adsorbates are captured in pairwise (J_{ij}), three-body (J_{ijk}), and higher-order terms, where the corresponding sums (eq 3) run over all of the sites. As illustrated in Figure 1, pairwise terms can span first-nearest-neighbor (1NN), second-nearest-neighbor (2NN), etc. separations. Three-body clusters can be linear or triangular of various shapes and sizes, and higher order clusters become increasingly diverse. Equation 3 can be simplified and written as the energy per site times the expected (averaged) value of the spin product (also known as the correlation) of all of the vertices for a given figure across all locations (eq 4):

$$E_{\text{CE}}(\sigma)/N_{\text{sites}} = \sum_{\text{figures}} m_a J_a \left\langle \prod_j^{\text{figure}_a} \sigma_j \right\rangle \quad (4)$$

Here, m_a is the multiplicity (number of symmetry equivalent rotations and reflections) of the figure. The unknown ECI can be fit to the DFT energy/configuration database using a least-squares algorithm. The infinite basis set of figures is complete

and orthogonal so that the expansion is exact in that limit.³⁵ For a finite-sized database, the practical challenge is to choose a compact set of figures that represents the energies reliably without introducing artifacts of overfitting. Once parametrized, the cluster expansion can be used to rapidly calculate the energy of any arbitrary adsorbate configuration.

Several CEs have been reported for the fcc Pt(111)–O system^{20–22} based on fittings to the DFT energies of a relatively small number (15 to 16) of O configurations. Each of these CEs captures the $p(2 \times 2)$ -O and $p(2 \times 1)$ -O ground state configurations and predicts a $p(\sqrt{3} \times \sqrt{3})$ -2O ground state configuration but differ in their predictions of other ground states. While the CEs are typically fit to formation energies relative to the clean Pt(111) surface and oxygen (either as a full ML on the Pt(111) surface or as O₂ in a vacuum), a common application of the CE is the calculation of energy differences corresponding to the addition or removal of a single adsorbate. Such models have been used in Monte Carlo simulations to predict surface adsorbate phase diagrams^{20,21} and recently to model coverage-dependent kinetic phenomena.³⁶ To date, however, a detailed comparison of the performance of the CEs for formation and differential adsorption energies has not been carried out.

Here, we report an extensive DFT database of 66 Pt(111)–O configurations in supercells ranging from 1 to 16 unique adsorption sites. We fit this database of formation energies to a range of CEs of systematically increasing size and flexibility. We find that the performance of the CE depends upon the property or properties of interest. More specifically, ground states and formation energies can be predicted reliably with moderate-sized CEs, but differential adsorption energies require larger CEs to achieve the same accuracy. The choice of figures in cluster expansions is also examined. It is found that many figures are interchangeable but that short-ranged pairwise figures as well as the linear 1–1–3 triplet (Figure 1) are necessary to obtain CEs that correctly capture the qualitative features of the Pt(111)/O system. Additionally, strain effects are studied by isolating the electronic effects in a CE of a database of formation energies for unrelaxed configurations. Interactions are shorter ranged and more repulsive at a 1NN separation in the unrelaxed configurations; adsorbate-induced surface strain is responsible for longer-ranged repulsions and contributes a 1NN attractive interaction that decreases, but does not overcome, the intrinsic electronic 1NN repulsion.

2. COMPUTATIONAL METHODS

We used the Vienna ab initio package (VASP)^{37–40} to perform plane-wave, supercell DFT calculations within the PW91 implementation of the generalized gradient approximation (GGA)⁴¹ and a projector augmented wave (PAW) treatment of core electronic states.^{42,37,39,40} Plane waves were included in the DFT calculations to an energy cutoff of 400 eV. Bulk Pt energy calculations were performed on unit face centered cubic (fcc) cells with a well-converged $30 \times 30 \times 30$ Γ -centered k -point mesh. The lattice constants of these cells were uniformly distributed near the experimental value of 3.912 Å.⁴³ Fitting these energies to the Birch–Murnaghan equation of state^{44,45} yields a computed lattice constant of 3.986 Å, which is used to determine the dimensions of supercells in the subsequent slab calculations. Pt(111) surface calculations were performed using a slab model consisting of four Pt layers, an atomic oxygen adsorbate layer, and four vacuum layers (Figure 2). The bottom Pt layer was fixed, and

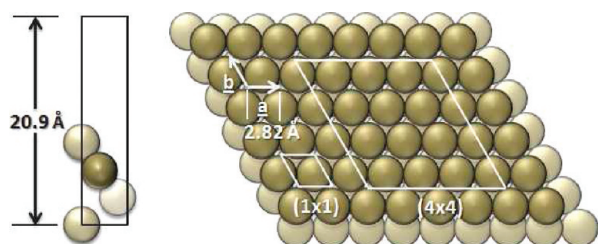


Figure 2. Side and top views of the smallest (1×1) periodic cell as well as the top view of the largest (4×4) periodic cell and unit vectors.

the remaining layers were relaxed. For comparison, we calculated DFT formation energies of the $p(2 \times 1)$ -O and full ML configurations using seven Pt layers and the bottom layer fixed, and with four Pt layers and the bottom two layers fixed. Formation energies differed by less than 4 meV/O. A Γ -centered k -point mesh with at least 85 k points per \AA^{-3} was used. O atoms were displaced from high symmetry positions and relaxed until the energy difference between subsequent optimization steps was less than 0.1 meV. Single point (no ionic relaxations) energy calculations were done using the tetrahedron method with Blöchl corrections⁴⁶ to determine final relaxed GGA energies. The effect of dipole corrections was tested on the clean, $p(2 \times 1)$ -O, and full ML configurations using a compensating dipole sheet at the center of the vacuum and parallel to the surface, as implemented in the VASP code.⁴⁰ Formation energy differences were only 1.0 and 2.5 meV/site for the $p(2 \times 1)$ -O and full ML surfaces, respectively, reflecting the small dipole of the Pt–O bond. Fitted energies do not include dipole corrections.

We calculated the bond length and GGA energy of triplet molecular oxygen in a $20 \times 20 \times 20$ supercell to be 1.225 Å and -9.8 eV/ O_2 , respectively. The harmonic vibrational frequency, calculated by finite difference on the forces using displacements of 0.01 Å, was calculated to be 1550 cm^{-1} . Both the bond length and frequency are close to the experimental values of 1.208 Å⁴⁷ and 1556 cm^{-1} ,⁴⁸ respectively. For comparison, the molecular O_2 energy was also calculated from the experimental heat of formation of gaseous water extrapolated to 0 K ($H_{0,\text{H}_2\text{O}}^{\text{F}}$),⁴⁹ and the zero-point corrected GGA energies of H_2O and H_2 ($E_{0,i}$) were calculated in $20 \times 20 \times 20$ supercells with an energy cutoff of 700 eV:

$$E_{0,\text{O}_2} = E_{0,\text{H}_2\text{O}} - H_{0,\text{H}_2\text{O}}^{\text{F}} + E_{0,\text{H}_2} \quad (5)$$

The H_2 vibrational frequency is 4161 cm^{-1} ⁵⁰ and those of water are 3657, 1595, and 3756 cm^{-1} .⁴⁹ The O_2 energy calculated this way is -9.5 eV/ O_2 . The difference between the two references of 0.2 eV/O (0.3 eV/ O_2) reflects the intrinsic uncertainty in the GGA oxygen energy. We use the O_2 reference in the results reported here. The opposite choice would uniformly shift all energies by 0.2 eV/O. Relative errors for atomic oxygen on the Pt(111) surface are expected to be significantly less as GGA DFT energies are able to correctly predict the phase behavior.^{12,20–22} The error due to the uncertainty in the oxygen reference only affects the empty and point figures in any CE containing both of these figures, such that

$$\delta J_e = \frac{1}{4} \delta E_{\text{O}_2} \quad (6)$$

$$\delta J_p = -\frac{1}{4} \delta E_{\text{O}_2} \quad (7)$$

δJ_e and δJ_p are the uncertainties in the empty and point ECIs due to the uncertainty in the oxygen reference, δE_{O_2} . This relation can be derived by setting $(\theta/2)\delta E_{\text{O}_2}$ equal to the cluster expansion Hamiltonian (eq 3). Pair and higher order terms are not affected by any DFT error in E_{O_2} .

A series of cluster expansions of the adsorbate formation energies was constructed from the DFT oxygen energy database (see eq 9 in section 3.1) by considering up to 10th nearest neighbor (10NN) pairs (the largest supercell was 11.3 Å by 11.3 Å), triplets with a single site up to 5NN separation, and larger figures with up to six sites and no two sites separated by more than a 3NN distance. This yielded a candidate set of 10 pair, 29 triplet, 10 quadruplet, 7 quintuplet, and 4 sextuplet figures. Multiple steepest descent sweeps, with various sets of starting figures, were used to search for cluster expansions with the smallest errors. Tools from the Alloy Theoretic Automated Toolkit (ATAT) were used to calculate cross-validation (cv) scores for the steepest descent.^{26,27,51}

3. RESULTS

3.1. DFT Database. The structures and DFT energies of a total of 66 relaxed configurations of fcc atomic oxygen on Pt(111) were computed at coverages between 0 and 1 ML. These configurations were selected iteratively, starting from the smallest ordered structures and adding more complicated ones based on predictions from the CEs.^{26,27,51} In all cases, adsorbed O remains in fcc sites during optimization and the surface Pt remains near the same surface plane. Configurations and energies are included in the Supporting Information.

To compare the stabilities of these configurations, we first calculate the zero-point corrected DFT formation energy, $E_f(\sigma)$, per site relative to the clean surface and molecular O_2 :

$$\text{Pt}(111) + \frac{\theta}{2} \text{O}_2 \rightarrow \text{Pt}(111) - \text{O}(\sigma) \quad (8)$$

$$E_f(\sigma) = \frac{E_0(\sigma) - E_0(0)}{N} - \frac{\theta}{2} E_{0,\text{O}_2} \quad (9)$$

$E_0(\sigma)$ is the zero-point corrected DFT energy of configuration σ . $E_0(0)$ is the energy of the clean surface calculated in an identical supercell. N is the number of fcc surface sites in the supercell. $\theta = N_{\text{O}}/N$ is the oxygen coverage of the configuration, and E_{0,O_2} is the zero-point corrected DFT energy of O_2 . We neglect the minor changes in the Pt vibrational spectrum with adsorption and include vibrational contributions of adsorbed O, assuming these to be independent of coverage. DFT-calculated vibrational frequencies for an adsorbed O in a $p(4 \times 4)$ supercell are 429, 380, and 377 cm^{-1} ,¹² similar to the experimental values of 480 and 400 (doubly degenerate) cm^{-1} .¹⁴ The zero-point correction is thus linear in coverage and contributes 0.15 eV/O. Even with the dense k -point sampling used here, we find that it is important to construct energy differences between identically sized supercells to maximize error cancelation; otherwise, slight variations in the per site $E_0(0)$ with supercell size and shape lead to spurious predictions of relative energies and of ground states that propagate into errors in the CE fitting.

Figure 3a plots the GGA-computed formation energies (eq 9) vs O coverage. The convex hull connecting the stable ground-state configurations is indicated with a line, and configurations along the hull are sketched in Figure 4, including the corresponding periodic supercell. The negative initial slope of the hull reflects

exothermic dissociative O_2 adsorption at low coverage, and the upward curvature reflects the repulsive interactions between adsorbates. Notable are the numerous configurations near but not breaking the convex hull.¹² The large number of configurations

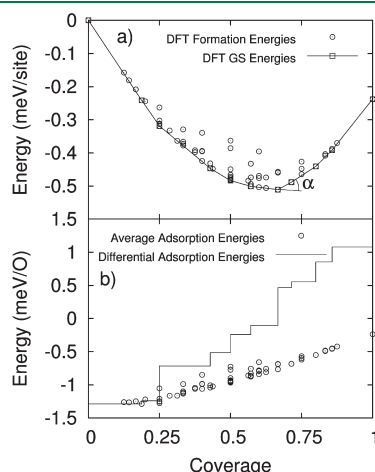


Figure 3. (a) DFT formation energies ($E_F(\sigma)$) for the fcc O/vacancy system on Pt(111). Ground-state configurations are highlighted and connected by lines. The definition of the hull exterior angle, α , is indicated. (b) DFT differential ($\epsilon_{\text{Ads}}(\sigma_1, \sigma_2)$) and average ($E_{\text{Ads}}(\sigma)$) adsorption energies.

close to or on the convex hull suggests, at practically relevant temperatures and coverages away from the strong ground states, that no one configuration will dominate the surface and, instead, regions of coexistence and/or disorder will dominate.

Table 1 summarizes the coverages and symmetries (following the 1996 IUPAC convention)⁵² of the computed ground states. To quantify the extent to which the various ground states break the convex hull, we calculate the hull exterior angle α , defined as the exterior angle minus 180° (Figure 3a). Prominent ground states with large exterior angles include the experimentally observed $p(2 \times 2)$ -O ordering (Figure 4c), in which all O atoms are equivalent and third-nearest neighbor to one another, and $p(2 \times 1)$ -O ordering (Figure 4e), in which O atoms form first-nearest-neighbor rows separated by empty rows.¹² The $p(\sqrt{3} \times \sqrt{3})$ -2O ground state (Figure 4g) has a hexagonal symmetry and the largest hull exterior angle of all ground states. The $3/7$ and $4/7$ ML configurations (Figure 4d and f) have α values close to that of the $p(2 \times 1)$ -O one and present similar rows of first-nearest-neighbor separated O. In the $3/7$ ML configuration, rows of length three are offset by the $p(100)$ vector, so that the row ends are at second-nearest-neighbor separations. In the $4/7$ ML configuration, these rows are of length four, offset by the $p(110)$ vector, so that all row ends are at first-nearest-neighbor separations. These two configurations are interesting in that not all adsorbed O atoms are equivalent. A similar structure at $2/5$ ML containing $p(2 \times 1)$ -O rows of length two was identified as a ground state in a previous DFT study.²¹ We calculate the

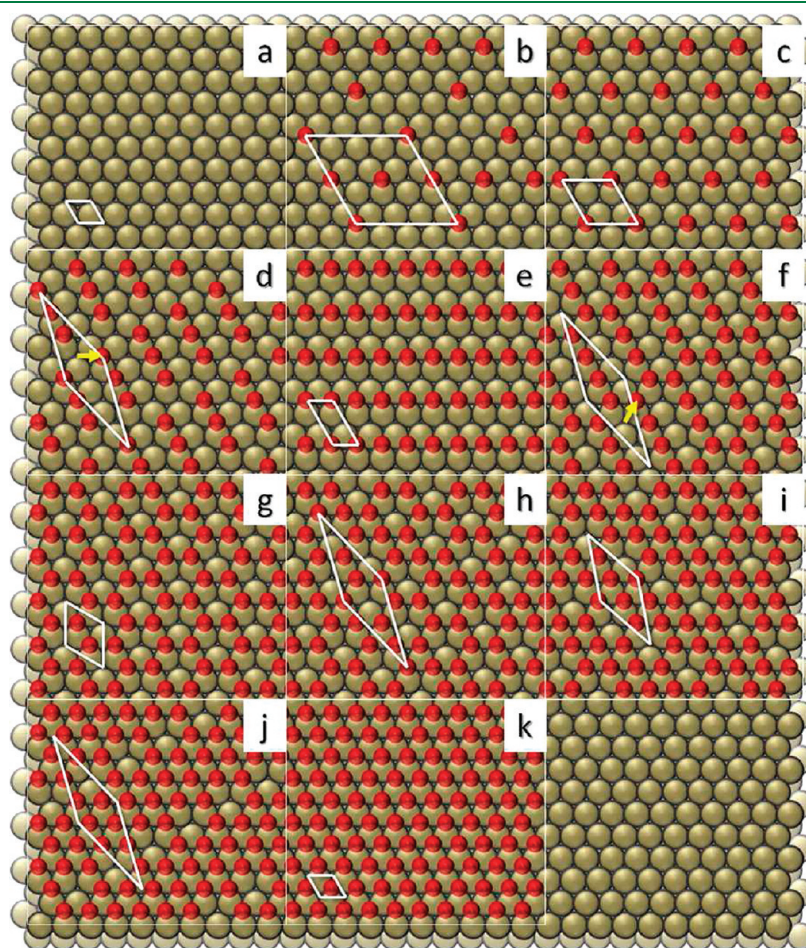


Figure 4. Ground state configurations and periodic supercells in the fcc O/vacancy system on Pt(111). See Table 1 for symmetries.

Table 1. DFT-Computed Ground State Configurations and Hull Exterior Angles, α

| | coverage (ML) | α (deg) | symmetry |
|-----|---------------|----------------|---|
| (b) | 3/16 | 3 | $p(4 \times 4)\text{-}3\text{O}$ |
| (c) | 1/4 | 28 | $p(2 \times 2)\text{-O}$ |
| (d) | 3/7 | 11 | $\begin{pmatrix} 1 & 3 \\ -1 & 4 \end{pmatrix} - 3\text{O}$ |
| (e) | 1/2 | 15 | $p(2 \times 1)\text{-O}$ |
| (f) | 4/7 | 8 | $\begin{pmatrix} 1 & 3 \\ -1 & 4 \end{pmatrix} - 4\text{O}$ |
| (g) | 2/3 | 30 | $(\sqrt{3} \times \sqrt{3})\text{R}30^\circ - 2\text{O}$ |
| (h) | 5/7 | 5 | $\begin{pmatrix} 1 & 3 \\ -1 & 4 \end{pmatrix} - 5\text{O}$ |
| (i) | 4/5 | 17 | $\begin{pmatrix} 1 & 3 \\ -1 & 4 \end{pmatrix} - 4\text{O}$ |
| (j) | 6/7 | 13 | $\begin{pmatrix} 1 & 3 \\ -1 & 4 \end{pmatrix} - 6\text{O}$ |

2/5 ML structure to lie just above the computed convex hull. Because of the similarity between all of these structures and the $p(2 \times 1)\text{-O}$ configuration, it may be difficult to distinguish these in LEED or STM experiments; nonetheless, their appearance has implications for surface adsorption energies.

The average adsorption energy, $E_{\text{ads}}(\sigma)$, per oxygen is related to the formation energy by the coverage, θ :

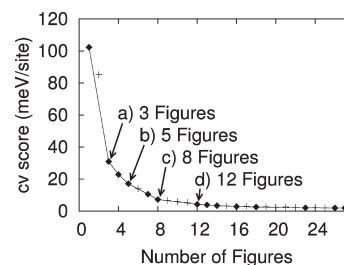
$$E_{\text{ads}}(\sigma) = \frac{E_{\text{F}}(\sigma)}{\theta} \quad (10)$$

Figure 3b plots the GGA-computed E_{ads} vs coverage. The low coverage limiting adsorption energy is computed to be -1.3 eV per O using the GGA O_2 reference (-1.5 eV per O using the GGA $\text{H}_2\text{O}/\text{H}_2$ reference), which can be compared to the -1.1 eV/O inferred from an analysis of oxygen TPD.^{17,18,53} Calorimetric measurements yield a more exothermic value of -1.6 eV/O.¹⁹ Above 1/4 ML, the average energy rises gradually, again reflecting accumulated repulsive interactions between adsorbates. The differential adsorption energy (ε_{ads}) between subsequent ground states σ_1 and σ_2 is the slope of the connecting convex hull, or equivalently the difference in formation energy divided by the difference in coverage:

$$\varepsilon_{\text{ads}}(\sigma_1, \sigma_2) = \frac{E_{\text{F}}(\sigma_1) - E_{\text{F}}(\sigma_2)}{\theta(\sigma_1) - \theta(\sigma_2)} \quad (11)$$

GGA-calculated differential adsorption energies are plotted as the staircase in Figure 3b. ε_{ads} is equivalent to E_{ads} at low coverage but exhibits discontinuous jumps at the ground states of heights related to the hull exterior angle. The differential adsorption energy becomes significantly positive at 2/3 ML coverage; even with a generous estimate of the GGA error, O_2 dissociation into fcc sites is predicted to become endothermic above this 2/3 ML coverage.

3.2. Cluster Expansions. We next fit the oxygen adsorbate formation energy DFT database to a set of cluster expansion models. While in principle the infinite cluster expansion is exact, in practice the expansion must be truncated at some finite number

**Figure 5.** Cross validation (meV/site) score versus number of figures.

of terms, and the selection of an optimal set of fitting figures is one of the primary challenges to the CE approach.^{22,35} The most common measure of the predictive capability of a CE is the leave-one-out cross-validation, or CV score.^{20–22,26–29,32} For a given set of basis figures, the effective cluster interactions (ECIs) are determined by least-squares fitting to all but one of the DFT formation energies and the prediction error in the one excluded configuration determined. This predicted error is calculated for every configuration in the DFT database and the root-mean-square (RMS) value of all errors is the CV score:²⁶

$$\text{CV} = \sqrt{\langle (E_{\text{s}}^{\text{CE}}(\sigma) - E_{\text{F}}(\sigma))^2 \rangle} \quad (12)$$

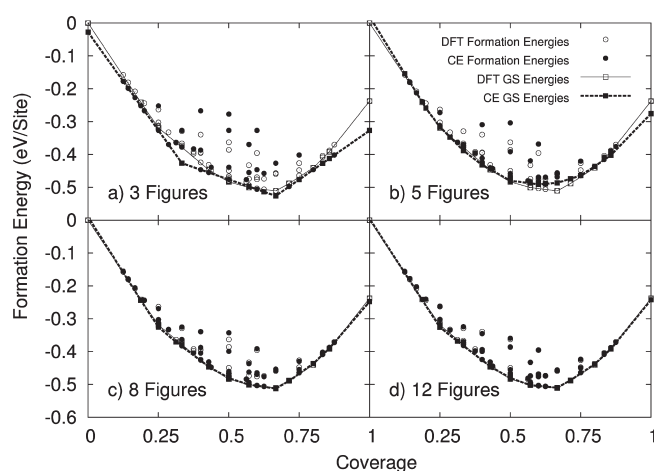
Here, $E_{\text{s}}^{\text{CE}}(\sigma)$ is the predicted energy per site of configuration σ , excluding that configuration from the fit, and $E_{\text{F}}(\sigma)$ is the corresponding DFT-calculated formation energy. Our candidate set of figures included pair, triplet, quadruplet, quintuplet, and sextuplet figures as discussed in section 2. We built up successively larger cluster expansions using steepest descent searches in which each subsequent addition or removal of a figure is done by searching over all possible candidates, adding or removing the figure that maximally decreases the CV score. To overcome local minima in this search procedure, the addition and/or removal of two figures simultaneously was performed when this resulted in a lower CV score. The result of this search is shown in Figure 5, plotted as CV score vs number of symmetry-distinct figures. Analogous to the formation energies, a “convex hull” of CEs can be identified, where kinks represent significant changes in the efficiency of the CE for predicting formation energies.

The lowest cv score did not always monotonically decrease as the number of configurations in the DFT database grew. The cv score typically decreased on the order of 1 meV/site but occasionally increased significantly as new oxygen configurations expanded configuration space. The cv score did monotonically decrease after the database reached 25 oxygen configurations, suggesting that the relevant configuration space had been covered. The iterative DFT and CE procedure provides a valuable self-consistency check: we were able to identify several miscalculated DFT energies by the inability to fit the energies and associated configurations within a CE.

The CE representation of the Langmuir model (eq 1) would include only empty and point terms and, given the relatively strong adsorbate interactions in the Pt(111)/O system, such a model has a very large cv score of 85 meV/site. Table 2 shows the computed ECIs for a CE that adds the 1NN figure (Figure 1), the CE at the first kink in Figure 5. (For counting purposes, we term this a “3 figure” CE, identifying the empty and point as the first and second figures). This 1NN pairwise term has a large positive ECI that strongly disfavors 1NN O pairs and improves the cv score to 31 meV/site. A 3 figure CE with empty, point, and 1NN

Table 2. Effective Cluster Interactions (ECI) for Four Cluster Expansions

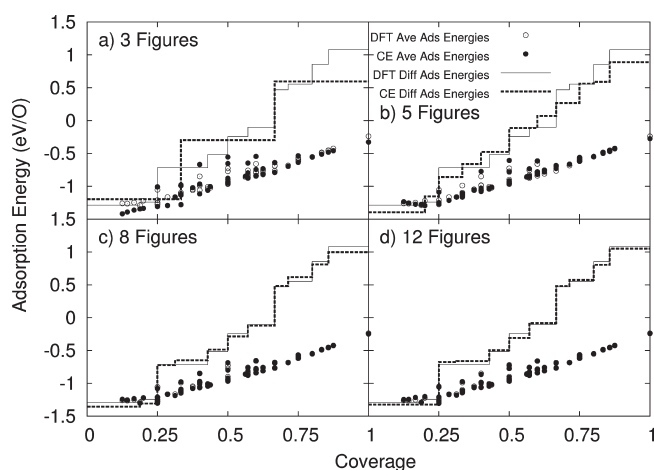
| figure | ECI (meV/site) | | | |
|--------|----------------|-------------|-------------|--------------|
| | 3 figure CE | 5 figure CE | 8 figure CE | 12 figure CE |
| empty | −402 | −424 | −423 | −426 |
| point | −150 | −148 | −153 | −159 |
| 1NN | 75 | 65 | 55 | 53 |
| 2NN | | 21 | 14 | 12 |
| 3NN | | 21 | 11 | 7 |
| 4NN | | | 7 | 7 |
| 5NN | | | 7 | 8 |
| 6NN | | | | 3 |
| 7NN | | | | 2 |
| 8NN | | | | 3 |
| 1–1–3 | | | 8 | 7 |
| 1–2–3b | | | | 2 |

**Figure 6.** Cluster expansion fitted and DFT formation energies of four CEs of increasing size.

figures can only predict ground states at 0, 1/3, 2/3, and 1 ML coverage and therefore cannot predict the proper phase behavior for dissociative oxygen adsorption on Pt(111).⁵⁴

The 2NN and then 3NN pairs are the two next most important figures found in the CE search, and CEs adding these two appear as kinks at 23 and 17 meV/site in Figure 5, respectively. These terms also have positive ECIs that again disfavor O at these separations. While these two-body terms are the most important O–O interactions,¹² pairwise figures alone are not able to reproduce the asymmetry in the ground state configurations about 1/2 ML. Figure 6a contrasts the DFT-computed formation energies with those predicted by the 3-figure CE. This 3-figure CE fails to reproduce the ground state at 1/4 ML coverage, predicts a spurious ground state at 1/3 ML, predicts incorrect ground state oxygen configurations at 3/7 and 4/7 ML, and errs seriously in the energies of many of the nonground-state configurations. The 5-figure CE in Figure 6b improves the energy predictions significantly in most cases and predicts correct ground states at 3/7 and 4/7 ML but produces unphysical ground states at 1/3 ML and 3/4 ML.

These difficulties are reflected in the CE-computed average and differential adsorption energies, shown in Figure 7. Average

**Figure 7.** Cluster expansion fitted and DFT, average, and differential adsorption energies plotted against coverage for 3 figure CE, 5 figure CE, 8 figure CE, and 12 figure CE.

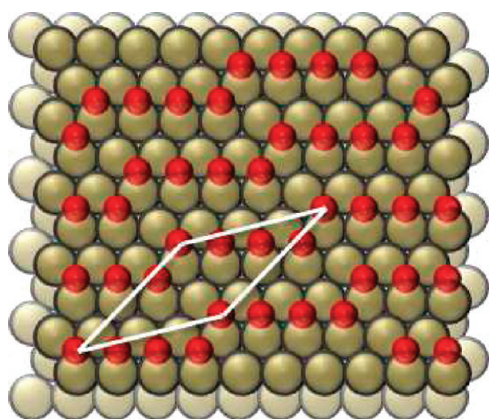
adsorption energies are captured within 0.19 eV/O for most configurations even in the 3 figure CE; the 5 figure CE reduces the largest errors to 0.13 eV/O. In contrast, because of errors in the ground state predictions, differential adsorption energies are reproduced much less well, with errors up to 0.5 eV/O at some coverages in the 3 figure CE and 0.3 eV/O in the 5 figure CE. In general, pairwise only models are not able to quantitatively reproduce coverage-dependent energies or equilibrium configurations of O on Pt(111).

The next minor kink in the cv vs figure search is at a seven figure CE that adds the 1–1–3 linear triplet and the fourth-nearest-neighbor (4NN) pair figure (Figure 1), decreasing the cv score to 10.5 meV/site. Adding the fifth-NN pair produces a strong kink in Figure 5 at an eight-figure CE with a CV score of 7.2 meV/site. The figures in this 8-figure CE are identical to the Pt(111)–O figures identified in another report.²⁰ As shown in Figure 6c, this eight-figure CE captures the energies of nearly all of the configurations near the ground state hull and deviates substantially only for a few configurations far from the hull. The worst fit configurations are striped ones with large numbers of 1NN O–O and vacant site–vacant site pairs. As shown in Figure 7, this 8-figure CE captures average adsorption energies within 40 meV/O for all configurations. The locations of the steps in the differential formation energies are identified correctly, and differential adsorption energy errors are less than 84 meV/O.

It is interesting to consider the role of the 1–1–3 linear triplet in the Pt(111)/O system. A triplet or larger odd-bodied figure is necessary for introducing asymmetry into the ground state predictions. In introducing the asymmetry, the 1–1–3 linear triplet helps capture the prominent $p(\sqrt{3} \times \sqrt{3})\text{-}2\text{O}$ and $p(2 \times 2)\text{-O}$ configurations without disfavoring the $p(2 \times 1)\text{-O}$ ground state configuration. The 1–1–3 correlations (average spin product, see eq 4) are -1 , $-1/2$, and 0 for the $p(\sqrt{3} \times \sqrt{3})\text{-}2\text{O}$, $p(2 \times 2)\text{-O}$, and $p(2 \times 1)\text{-O}$ configurations, respectively, allowing a positive ECI value to favor the $p(2 \times 2)\text{-O}$ ground state over the $p(2 \times 2)\text{-}3\text{O}$ configuration (their correlations are necessarily opposite for odd-bodied figures) and the $p(\sqrt{3} \times \sqrt{3})\text{-}2\text{O}$ ground state over the $p(\sqrt{3} \times \sqrt{3})\text{-O}$ configuration, see Table 3. Any triplet must favor either the 3/7 or 4/7 ML ground state and disfavor the other for any nonzero correlation,

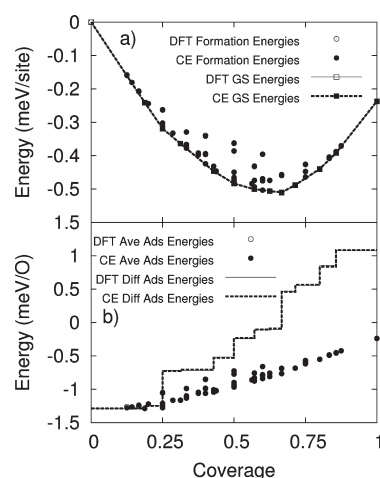
Table 3. Figure Correlations for the Most Prominent Ground States and Their Spin-Flipped Conjugates

| σ or θ | figure/correlation | | | | |
|----------------------|--------------------|--------|--------|-------|--------|
| | 1–1–3 | 1–1–1a | 1–1–1b | 1–1–2 | 1–2–3b |
| p(2 × 2)-O | −0.5 | 0.5 | 0.5 | 0.5 | −0.5 |
| p(√3 × √3)-O | 1 | 1 | 1 | −0.33 | −0.33 |
| 3/7 | 0.24 | 0.43 | 0.43 | −0.14 | 0.05 |
| p(2 × 1)-O | 0 | 0 | 0 | 0 | 0 |
| 4/7 | −0.24 | −0.43 | −0.43 | 0.14 | −0.05 |
| p(√3 × √3)-2O | −1 | −1 | −1 | 0.33 | 0.33 |
| p(2 × 2)-3O | 0.5 | −0.5 | −0.5 | −0.5 | 0.5 |

**Figure 8.** The 12-figure CE predicted ground state at 1/2 ML O.

as their correlations are necessarily opposite. The 1–1–3 triplet has a correlation of ± 0.24 for these ground states, relatively small compared to the correlations of the p(2 × 2)-O and p(√3 × √3)-2O ground states. Of the three previously published Pt(111)-O cluster expansions, all identified this linear 1–1–3 triplet as an important term.^{20–22} It is interesting to note that the most compact triplets, 1–1–1a and 1–1–1b in Figure 1, which differ as to whether they encompass an fcc or hcp hollow, do not appear in any of the CEs constructed in this work. The correlation for p(√3 × √3)-2O is −1 for both 1–1–1 triplets, while the correlation for p(2 × 2)-O is 1/2 for both triplets. Because these are opposite in sign, any nonzero value of the ECI disfavors one or the other of these two ground states. Similarly, these triplets have moderate correlations of $\pm 3/7$ for the ground states at 3/7 and 4/7 ML.

Four more figures are added to reach the next significant kink in Figure 5, including the 6NN to 8NN pairs along with either the 1–2–3b or 1–1–2 triplet, depending on the exact figure selection procedure. The ECIs for all of these additional figures are 3 meV or less. As shown in Figure 6d, the 12-figure CE captures the formation energies of essentially all 66 configurations within the uncertainty of the DFT model, with greatest improvements in formation energy for configurations that are furthest from the hull. This 12-figure CE captures the high-energy, striped configurations much better than the 8-figure CE. These improvements come at a cost, however: this 12-figure CE predicts the configuration shown in Figure 8 to be 2.5 meV/site lower in energy than the p(2 × 1)-O one, opposite the 3.4 meV/site higher predicted by the DFT. As shown in Figure 7, the 12-figure

**Figure 9.** DFT and 27-figure cluster expansion (a) formation energies and (b) adsorption energies.

CE reproduces average adsorption energies essentially quantitatively (up to 0.03 eV/O error) and differential formation energies with a maximum error of 0.08 eV/O.

Neither 1–2–3b nor 1–1–2 triplet promote the prominent p(2 × 2)-O, p(2 × 1)-O, and p(√3 × √3)-2O ground state structures. The 1–2–3b triplet correlations have opposite signs for the p(2 × 2)-O and p(√3 × √3)-2O ground states and therefore cannot promote both ground states, and the 1–1–2 triplet is fit such that the p(2 × 2)-O and p(√3 × √3)-2O ground states are less energetically favorable. Both triplets have correlations of 0 for the p(2 × 1)-O configuration. As these triplets do not favor the ground states, the main contribution of these triplets appears to be in better fitting with the high energy, striped configurations.

Successively adding figures beyond the 12-figure expansion produces a series of CEs with slowly decreasing CV scores. No qualitatively significant new figures appear in this search. The largest CE constructed here has 27 figures and a CV score of 1.9 meV per site. The ECI for this 27-figure CE are included in the Supporting Information. Figure 9a compares computed and predicted formation energies and Figure 9b the average and differential adsorption energies vs O coverage. This 27-figure CE reproduces all quantities essentially quantitatively (maximum error of 0.02 eV/O). The power of the CE is in its ability to quickly predict energies for adsorbate configurations too numerous or large to practically calculate with DFT. To illustrate this predictive ability, 20 468 O configurations with up to 15 surface sites were generated using the ATAT and formation, average adsorption, and differential adsorption energies predicted. The results are shown in Figure 10. The general shape of the formation energy hull is preserved, but as readily seen, there are very many configurations that appear near the hull. These configurations correspond to various defects in the perfectly ordered configurations. New ground states do appear on the convex hull; however, these ground states have α angles less than 10° and break the convex hull by only a few millielectronvolts.

3.3. Surface Strain Effects. The effects of surface strain on adsorbate binding energies have been investigated experimentally and with first principle approaches.^{55–58} Surfaces under expansion bind adsorbates more exothermically,^{55,56} while surfaces under compression bind adsorbate less exothermically.⁵⁶ It has also been seen that adsorbates, including atomic oxygen,

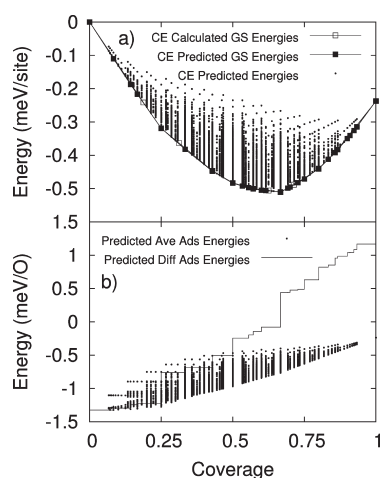


Figure 10. The 27-figure CE predicted (a) formation energies and (b) adsorption energies. No new ground states predicted with $\alpha > 10^\circ$.

induce strain in surfaces;^{12,59} however, the role of strain on adsorbate–adsorbate interactions has not been reported. To examine the effects of strain in adsorbate–adsorbate interactions, we evaluated the energies for a smaller database of atomic oxygen adsorbate configurations in which the platinum atoms are fixed at their clean surface positions and oxygen atoms are fixed in their full ML positions. (Separate tests showed that fixing or relaxing the O atoms had a small effect on the energies and no consequences for the conclusions here.)

The GGA formation energies for the fixed system are shown in Figure 11. The formation energies of the fixed system are similar to the relaxed system in that dissociative O_2 adsorption is exothermic at low coverage, the interactions are generally repulsive, as seen by the upward curvature of the convex hull, and ground states with large α angles exist at 1/4, 1/2, and 2/3 ML coverage. The formation energies are different in that O_2 adsorption is less exothermic than the relaxed system, ground states with large α angles are predicted at 1/3 and 3/4 ML coverage, minor ground states have appeared and disappeared at various other coverages, and there is generally more symmetry about 1/2 ML coverage.

We fitted these fixed Pt GGA energies to a CE following the procedure above. A CE with only four figures (empty, point, 1NN, and 2NN) is able to capture the fixed Pt formation energies with a CV score of 12 meV/site. In contrast, the same-sized CE fits the relaxed surface energies much less well, yielding a CV score of 23 meV/site. Table 4 shows an optimized 19-figure CE of the fixed Pt energies with a CV score of 1.8 meV/site. From comparison with Table 2, both types of figures and the strengths of the corresponding ECIs change. The ECI of the 1NN pair interaction is 16 meV more repulsive in the fixed system than when the Pt's are allowed to relax; however, all other pairwise ECIs are significantly smaller. For example, the ECI of the 2NN pair dropped to 3 meV from 8 meV, and interestingly, the 3NN pair interaction goes from being a repulsive 7 meV to an attractive -4 meV. The optimized relaxed and fixed system CEs also have different multibodied figures. The 1–1–3 triplet, which is most important for the relaxed system, does not appear as an important figure in any of fixed Pt CEs we examined. Oddly, the multibodied figure that has the largest impact on the CV score is the most compact quintuplet, identified in Table 2 as 5(1)–(2) for the five 1NN and one 2NN separations in the figure. The fit of almost every oxygen configuration moderately improves with

Table 4. Effective Cluster Interactions (ECI) for Fixed System CE

| figure | ECI (meV) |
|----------------|-----------|
| empty | –310 |
| point | –117 |
| 1NN | 66 |
| 2NN | 3 |
| 3NN | –4 |
| 4NN | 6 |
| 5NN | 1 |
| 8NN | 1 |
| 1–1–1b | –2 |
| 2–2–2 | 4 |
| 3–3–3a | 1 |
| 1–4–4 | 1 |
| 5–5–5a | 1 |
| 5(1)–(2) | 2 |
| 2(1)–2(2)–2(3) | 1 |
| 2(1)–2(2)–2(3) | 1 |
| 7(1)–2(2)–(3) | 2 |
| 4(1)–4(2)–2(3) | –2 |
| 5(1)–2(2)–3(3) | 1 |

this quintuplet, the most noticeable improvements being for the ground state configurations at 1/3 and 2/3 ML coverage. The remaining multibodied figures fall into at least one of two categories, equilateral (or isosceles in one case) triangular figures or short-ranged figures with up to 3NN pairwise separations, but mostly 1NN and 2NN separations. Interactions are generally shifted from relatively long-ranged interactions, in the relaxed system, to short-ranged interactions in the fixed system.

The Pt–O bond has a modest dipole moment,⁶⁰ so that electrostatics contribute little to the interactions. The short range of the interactions in the fixed Pt case can be understood in terms of simple chemical unsaturation arguments.¹ When an atomic oxygen adsorbate is on the surface, it bonds with the nearest platinum atoms, quenching some of their chemical unsaturation. Because the nearest platinum atoms are less chemically unsaturated, other atoms (including 1NN adsorbates) bind to these nearest platinum atoms less exothermically. A second adsorbate, binding 1NN with respect to the first adsorbate, will share a Pt with the first adsorbate and bind less favorably than the first adsorbate; hence there is an effective 1NN repulsion. The next nearest platinum atoms are now more chemically unsaturated (since they are not bound as tightly to the nearest platinum atoms) and will bind more strongly to other atoms than they did without an adsorbate on the surface. However, each nearest Pt atom has nine neighboring Pt atoms (including subsurface atoms) compared to only three nearest platinum atoms, so the effect is much less pronounced for the next nearest Pt atoms. As changes in the chemical saturation are propagated outwardly in three dimensions, they rapidly decay such that adsorbate interactions, due to chemical saturation/unsaturation, are short-ranged.

We performed fixed and relaxed calculations on a 6×6 supercell of a single O at an FCC site. Relaxation of the surface lowers the energy by over 200 meV/O. Figure 12 shows that Pt's 1NN to O are uniformly displaced laterally,¹² causing a local expansion of the Pt–Pt bonds (shown with red triangles), while those farther away are compressed (shown with blue triangles).

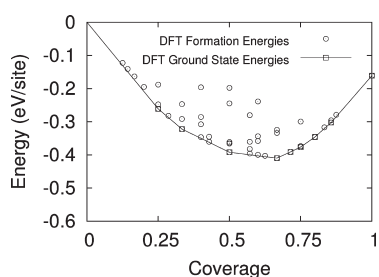


Figure 11. DFT formation energies for the fcc O/vacancy system on Pt(111) with platinum atoms fixed in clean surface locations. Ground-state configurations are highlighted and connected by lines.

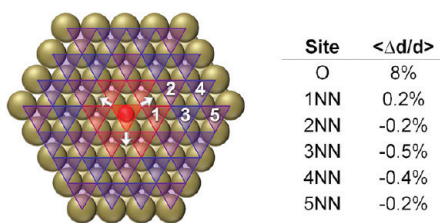


Figure 12. Single oxygen adsorbate on $p(6 \times 6)$ surface. Strain increases average Pt–Pt bond length locally (red triangles) and decreases remote average Pt–Pt bond lengths (blue triangles). The percent change of average Pt–Pt bond lengths around each type of site is shown in the inset table.

The inset table shows the average change in the Pt–Pt bond lengths around the adsorbed O and around each potential adsorption site up to 5NN from the adsorbed O. The O adsorbate induced strain increases the average Pt–Pt bond length by 8% for the Pt atoms around the O adsorbate and by 0.2% for the Pt atoms around the potential 1NN adsorption sites while decreasing the average Pt–Pt bond length by 0.2 to 0.5% for Pt atoms around the other potential adsorption sites. As strain is a long-range effect,^{61–65} strain-induced relaxations persist over longer distances than the chemical saturation/unsaturation effects.

As noted above, surfaces under compressive strain bind adsorbates less strongly, while those under expansion bind adsorbates more strongly.⁵⁶ Therefore, adsorbate-induced strain is attractive at 1NN and repulsive at longer distances. Comparing Tables 2 and 4 confirms this trend. The long-range, strain-induced repulsions increase the relative probability of adsorbates binding at 1NN, acting as a pseudoattraction.

4. CONCLUSIONS

DFT-fitted cluster expansions provide a general means of incorporating coverage dependence into models of surface adsorption. Here, we have examined the performance of a series of CEs for the Pt(111)–O system, drawing on a large DFT-computed database of configurational energies. We have compared cluster expansions of various sizes and examined their predictive capabilities for formation energies, average and differential adsorption energies, and ground states. Pair-wise cluster expansions poorly predict all properties investigated, but larger CEs fare better. It was found that adsorption energy errors are significantly larger than the formation energy errors (typically 100s of meV per O rather than up to 10 meV per site) but that sufficiently larger cluster expansions reduce these errors.

In comparing these cluster expansions, short pairwise interaction as well as the 1–1–3 linear triplet were found to be important for accurately predicting properties; however, the selection of other specific figures was less important.

Adsorption-induced surface strain contributes significantly to adsorbate–adsorbate interactions. Surface relaxations due to adsorbates put the surface under compressive strain. This compressive strain results in relatively long-ranged, repulsive interactions for adsorbates beyond 1NN separations but reduces the repulsive interaction of 1NN adsorbates due to short-ranged cooperative relaxations. From a thermodynamic perspective, the long-ranged repulsions increase the probability of finding 1NN adsorbates, ironically acting as an additional pseudoattraction.

As alluded to in the Introduction, adsorbate–adsorbate interactions influence both the distributions/orderings of adsorbates at a surface as well as their adsorption energies. We have already demonstrated the ability of CEs to quickly calculate single oxygen, averaged, and differential adsorption energies. Additionally, the equilibrium spatial distributions of adsorbates at surfaces may be obtained using CEs coupled with the Monte Carlo method.²¹ The ability to precisely predict these quantities provides the foundation required for probing the quantity and type of energetically available dissociative O₂ adsorption sites, an avenue we are exploring to develop a better rate model for oxygen adsorption on the Pt(111) surface, and to gain insight into the types of dissociative O₂ adsorption sites that are available and important for catalytic oxidations and oxygen reduction reactions.³⁶

■ ASSOCIATED CONTENT

S Supporting Information. The DFT formation energy database, the ECI of the 27 figure CE, and a figure illustrating many-bodied interactions. This information is available free of charge via the Internet at <http://pubs.acs.org/>.

■ AUTHOR INFORMATION

Corresponding Author

*Phone: (574) 631-8754. Fax: (574) 631-8366. E-mail: wschneider@nd.edu

Notes

The authors declare no competing financial interest.

■ ACKNOWLEDGMENT

Valuable conversations with Dr. Chao Wu, Dr. Jean-Sabin McEwen, Dr. Zhengzheng Chen, and Jason Bray are gratefully acknowledged. Support for this work comes from the National Science Foundation under grant CBET-0731020 and CBET-0730841.

■ REFERENCES

- (1) Langmuir, I. *J. Am. Chem. Soc.* **1918**, *40*, 1361–1403.
- (2) Langmuir, I. *J. Am. Chem. Soc.* **1932**, *54*, 2798–2832.
- (3) Kreuzer, H.; Jun, Z.; Payne, S.; Nichtl-Pecher, W.; Hammer, L.; Müller, K. *Surf. Sci.* **1994**, *303*, 1–15.
- (4) Bligaard, T.; Norskov, J.; Dahl, S.; Matthiesen, J.; Christensen, C.; Sehested, J. *J. Catal.* **2004**, *224*, 206–217.
- (5) Iddir, H.; Fong, D.; Zapol, P.; Fuoss, P.; Curtiss, L.; Zhou, G.; Eastman, J. *Phys. Rev. B* **2007**, *76*, 241404.
- (6) Miller, D.; Öberg, H.; Näslund, L.; Anniyev, T.; Ogasawara, H.; Pettersson, L.; Nilsson, A. *J. Chem. Phys.* **2010**, *133*, 224701.
- (7) Shustorovich, E. *Surf. Sci. Rep.* **1986**, *6*, 1–63.

- (8) Shelef, M.; McCabe, R. *Catal. Today* **2000**, *62*, 35–50.
- (9) Gandhi, H.; Graham, G.; McCabe, R. *J. Catal.* **2003**, *216*, 433–442.
- (10) Epling, W.; Campbell, L.; Yezerets, A.; Currier, N.; Parks, J. *Catal. Rev. Sci. Eng.* **2004**, *46*, 163–245.
- (11) Getman, R.; Schneider, W. *J. Phys. Chem. C* **2007**, *111*, 389–397.
- (12) Getman, R.; Xu, Y.; Schneider, W. *J. Phys. Chem. C* **2008**, *112*, 9559–9572.
- (13) Markovic, N. M.; Schmidt, T. J.; Stamenkovic, V.; Ross, P. *Fuel Cells* **2001**, *1*, 105–116.
- (14) Steininger, H.; Lehwald, S.; Ibach, H. *Surf. Sci.* **1982**, *123*, 1–17.
- (15) Mortensen, K.; Klink, C.; Jensen, F.; Besenbacher, F.; Stensgaard, I. *Surf. Sci. Lett.* **1989**, *220*, L701–L708.
- (16) Hawkins, J.; Weaver, J.; Asthagiri, A. *Phys. Rev. B* **2009**, *79*, 125434.
- (17) Campbell, C.; Ertl, G.; Kuipers, H.; Segner, J. *Surf. Sci.* **1981**, *107*, 220–236.
- (18) Parker, D.; Bartram, M.; Koel, B. *Surf. Sci.* **1989**, *217*, 489–510.
- (19) Yeo, Y.; Vattuone, L.; King, D. *J. Chem. Phys.* **1997**, *106*, 392–401.
- (20) Han, B.; Van der Ven, A.; Ceder, G.; Hwang, B. *Phys. Rev. B* **2005**, *72*, 205409.
- (21) Tang, H.; Van der Ven, A.; Trout, B. *Phys. Rev. B* **2004**, *70*, 045420.
- (22) Miller, S.; Kitchin, J. *Mol. Simul.* **2009**, *35*, 920–927.
- (23) Devarajan, S.; Hinojosa, J., Jr.; Weaver, J. *Surf. Sci.* **2008**, *602*, 3116–3124.
- (24) Weaver, J.; Chen, J.; Gerrard, A. *Surf. Sci.* **2005**, *592*, 83–103.
- (25) Miller, S.; Kitchin, J. *Surf. Sci.* **2009**, *603*, 794–801.
- (26) Van de Walle, A.; Ceder, G. *J. Phase Equilib.* **2002**, *23*, 348–359.
- (27) Van de Walle, A.; Asta, M.; Ceder, G. *Calphad* **2002**, *26*, 539–553.
- (28) Lerch, D.; Wieckhorst, O.; Hart, G.; Forcade, R.; Müller, S. *Modell. Simul. Mater. Sci. Eng.* **2009**, *17*, 055003.
- (29) Lerch, D.; Wieckhorst, O.; Hammer, L.; Heinz, K.; Müller, S. *Phys. Rev. B* **2008**, *78*, 121405.
- (30) Stampfl, C.; Kreuzer, H.; Payne, S.; Pfnür, H.; Scheffler, M. *Phys. Rev. Lett.* **1999**, *83*, 2993–2996.
- (31) McEwen, J.; Payne, S.; Stampfl, C. *Chem. Phys. Lett.* **2002**, *361*, 317–320.
- (32) Lazo, C.; Keil, F. *Phys. Rev. B* **2009**, *79*, 245418.
- (33) Chen, W.; Schmidt, D.; Schneider, W.; Wolverton, C. *J. Phys. Chem. C* **2011**, *115*, 17915–17924.
- (34) Chen, W.; Wolverton, C.; Schmidt, D.; Schneider, W. *Phys. Rev. B* **2011**, *83*, 075415.
- (35) Sanchez, J.; Ducastelle, F.; Gratias, D. *Phys. A* **1984**, *128*, 334–350.
- (36) Wu, C.; Schmidt, D.; Wolverton, C.; Schneider, W. *F. J. Catal.* **2011** in press.
- (37) Kresse, G.; Furthmüller, J. *Comput. Mater. Sci.* **1996**, *6*, 15–50.
- (38) Kresse, G.; Furthmüller, J. *Phys. Rev. B* **1996**, *54*, 1169.
- (39) Kresse, G.; Joubert, D. *Phys. Rev. B* **1999**, *59*, 1759.
- (40) Kresse, G.; Furthmüller, J. *Vienna ab-initio simulation package (VASP): The guide*; Institut für Materialphysik: Universität Wien, Vienna, 2007.
- (41) Perdew, J.; Wang, Y. *Phys. Rev. B* **1992**, *45*, 13244.
- (42) Blöchl, P. *Phys. Rev. B* **1994**, *50*, 17953.
- (43) Davey, W. *Phys. Rev.* **1925**, *25*, 753–761.
- (44) Murnaghan, F. *Proc. Natl. Acad. Sci. U. S. A.* **1944**, *30*, 244–247.
- (45) Birch, F. *Phys. Rev.* **1947**, *71*, 809–824.
- (46) Blöchl, P.; Jepsen, O.; Andersen, O. *Phys. Rev. B* **1994**, *49*, 16223.
- (47) Sette, F.; Stöhr, J.; Hitchcock, A. *J. Chem. Phys.* **1984**, *81*, 4906–4914.
- (48) Weber, A.; McGinnis, E. *J. Mol. Spectrosc.* **1960**, *4*, 195–200.
- (49) Linstrom, P.; Mallard, W. In *NIST Chemistry WebBook*, NIST Standard Reference Database Number 69; Linstrom, P., Mallard, W., Eds.; National Institute of Standards and Technology: Gaithersburg, MD, 2010.
- (50) Stoicheff, B. *Can. J. Phys.* **1957**, *35*, 730–741.
- (51) van de Walle, A. *Alloy Theoretic Automated Toolkit (ATAT)*, 2.66 ed; Cal Tech: Pasadena, CA, 2008.
- (52) Bradshaw, A.; Richardson, N. *Pure Appl. Chem.* **1996**, *68*, 457–468.
- (53) Kreuzer, H.; Payne, S.; Drozdowski, A.; Menzel, D. *J. Chem. Phys.* **1999**, *110*, 6982–6999.
- (54) Schick, M.; Walker, J.; Wortis, M. *Phys. Rev. B* **1977**, *16*, 2205–2219.
- (55) Gsell, M.; Jakob, P.; Menzel, D. *Science* **1998**, *280*, 717–720.
- (56) Mavrikakis, M.; Hammer, B.; Nørskov, J. *Phys. Rev. Lett.* **1998**, *81*, 2819–2822.
- (57) Kitchin, J.; Nørskov, J.; Barteau, M.; Chen, J. *J. Chem. Phys.* **2004**, *120*, 10240–10246.
- (58) Kitchin, J.; Nørskov, J.; Barteau, M.; Chen, J. *Phys. Rev. Lett.* **2004**, *93*, 156801.
- (59) Ibach, H. *J. Vac. Sci. Technol., A* **1994**, *12*, 2240–2245.
- (60) Lin, X.; Ramer, N.; Rappe, A.; Hass, K.; Schneider, W.; Trout, B. *J. Phys. Chem. B* **2001**, *105*, 7739–7747.
- (61) Muller, S.; Wolverton, C.; Wang, L.; Zunger, A. *Phys. Rev. B* **1999**, *60*, 16448.
- (62) Ozolins, V.; Wolverton, C.; Zunger, A. *Phys. Rev. B* **1998**, *57*, 4816.
- (63) Ozolins, V.; Wolverton, C.; Zunger, A. *Phys. Rev. B* **1998**, *57*, 6427.
- (64) Wolverton, C.; Zunger, A. *Phys. Rev. Lett.* **1995**, *75*, 3162.
- (65) Laks, S.; Ferreira, L.; Froyen, S.; Zunger, A. *Phys. Rev. B* **1992**, *46*, 12587.